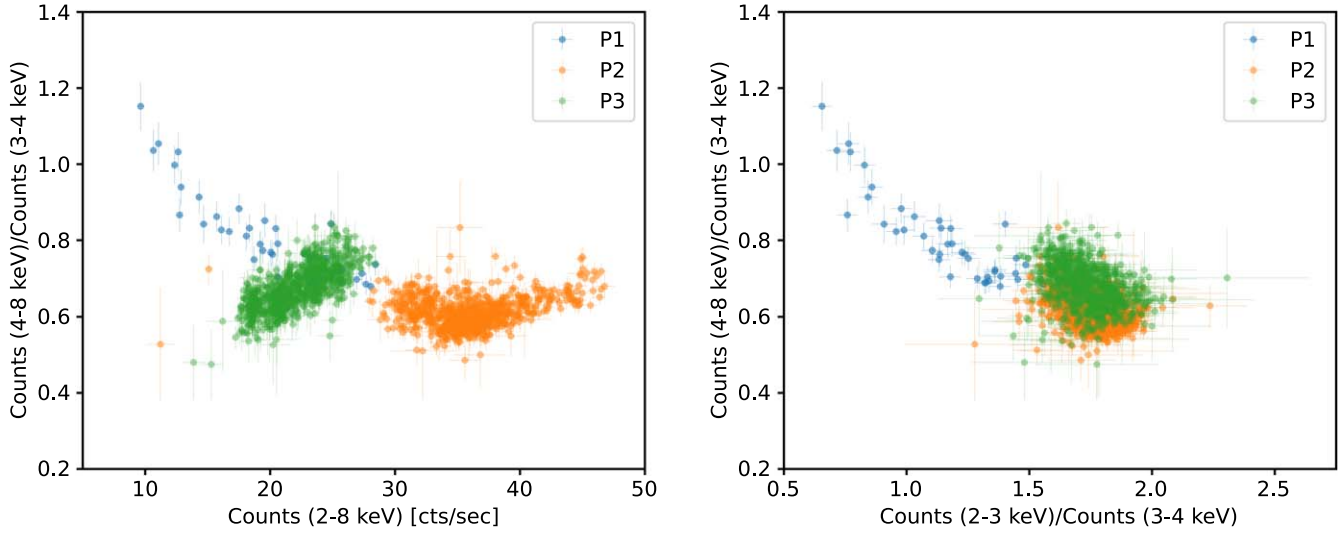

Figure 2. Hardness–intensity (left) and color–color (right) diagrams during the IXPE observations, binned in time bins of 180 s, with color highlighting the three phase intervals chosen for the subsequent analysis.

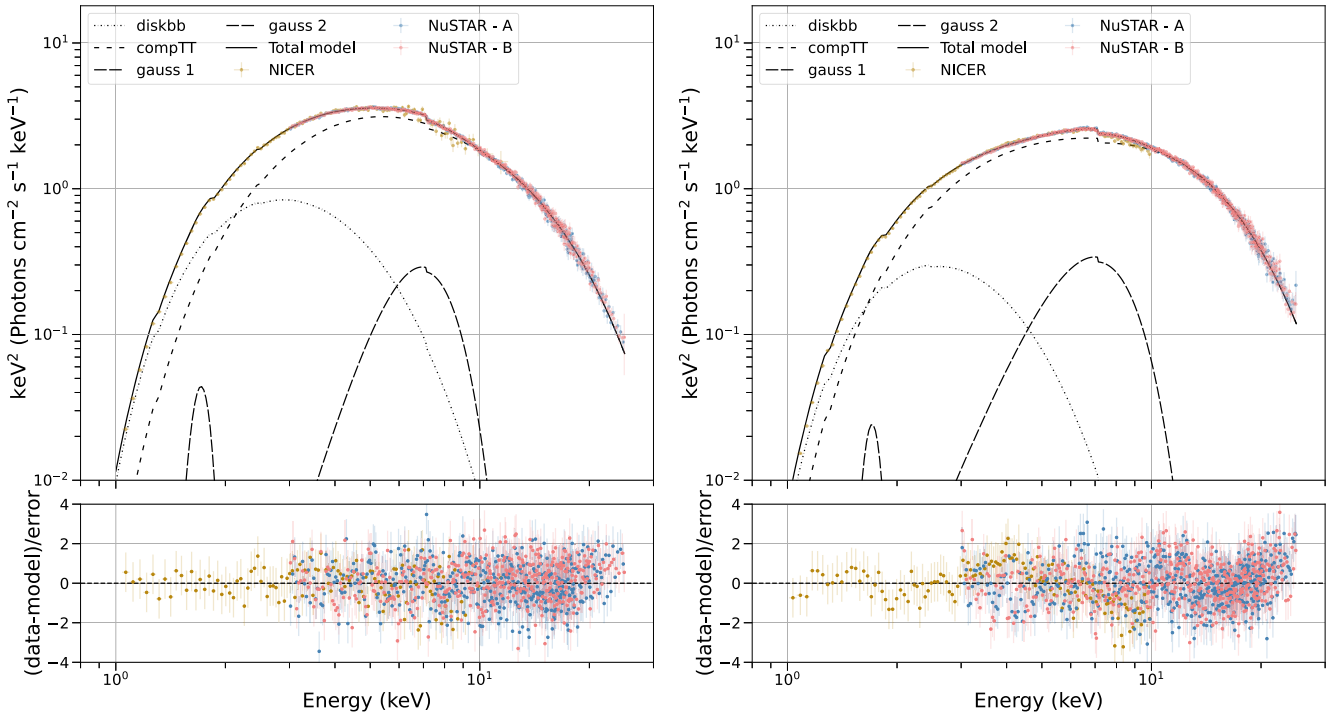

Figure 3. Spectral energy distribution of Cir X-1 during P2 (left) and P3 (right) in EF_E representation using NICER and NuSTAR (FPMA and FPMB) data and showing the different model components.

at the `wilm` values (Wilms et al. 2000); we started with a `tbabs` model but found that there were residuals better taken into account using `tbfeo`. The resulting model is written in XSPEC as `tbfeo*(diskbb+comptt+Gauss+Gauss)`.

We started by leaving all the parameters free but found the temperature of the disk to be degenerate with its norm. We then fixed the disk temperature to a value minimizing the χ^2 and left the norm free in the subsequent fit; the resulting best-fit models are shown in Figure 3, and the parameters are given in Table 2. We see that the flux during P3 is lower than in P2, and the spectrum is harder. This is also reflected in a significantly higher optical depth τ_p during P3, while the electron temperature is nearly the same. We left a free constant between NICER and NuSTAR, as well as between the different NuSTAR modules: the two NuSTAR modules, normalized to NICER, have values of 1.16 and 1.14 in P2 and 1.39 and 1.37 in P3. Since NuSTAR shows calibration uncertainties (Madsen et al. 2022), we left free a gain offset in the fit. No systematic errors were added to the fits (a known systematic error of $<1.5\%$ is already applied to NICER data by the NICER pipeline `nicerl3-spect`). From the relative fluxes of the components in the nominal IXPE energy band of 2–8 keV, we see that, even if both components are present, the dominant component is `comptt`. One of the Gaussians is an instrumental NICER feature, while the other is not visible due to a low IXPE energy resolution with respect to NICER and

Table 2
Best-fit Parameters of the Spectral Model `tbfeo*(diskbb+comptt +Gauss+Gauss)` Applied to the Simultaneous Data from NICER and NuSTAR

Model	Parameter	P2	P3
`tbfeo`	$N_{\rm H}$ (10^{22} cm^{-2})	$3.0^{+0.5}_{-0.8}$	$3.09^{+0.01}_{-0.31}$
	Fe (10^{22} cm^{-2})	<1.6	<0.3
	O (10^{22} cm^{-2})	$2.6^{+1.1}_{-0.6}$	$2.7^{+0.2}_{-0.3}$
`diskbb`	$kT_{\rm in}$ (keV)	0.85[a]	0.7[a]
	norm $([R_{\rm in}/D_{10}]^2 \cos\theta)$	417^{+32}_{-35}	360^{+12}_{-2}
`comptt`	kT_0 (keV)	1.00 ± 0.03	0.74 ± 0.01
	$kT_{\rm e}$ (keV)	$2.56^{+0.03}_{-0.02}$	$2.539^{+0.006}_{-0.003}$
	τ	$4.93^{+0.09}_{-0.12}$	$7.22^{+0.08}_{-0.02}$
	norm	0.68 ± 0.02	$0.50^{+0.01}_{-0.05}$
`Gauss`	$E_{\rm line}$ (keV)	6.5 ± 0.1	$6.04^{+0.01}_{-0.22}$
	σ (keV)	$1.27^{+0.07}_{-0.08}$	$1.75^{+0.01}_{-0.05}$
	norm (photon s^{-1} cm^{-2})	0.017 ± 0.003	0.034 ± 0.002
`Gauss`	$E_{\rm line}$ (keV)	1.7[a]	1.7[a]
	σ (keV)	0.08 ± 0.03	0.08[a]
	norm (photon s^{-1} cm^{-2})	0.009 ± 0.0003	0.005 ± 0.001
	χ^2/dof	$1271/1222 = 1.04$	$1398/1226 = 1.14$
	Photon flux in 2–8 keV		
	$F_{\rm tot}$ (10^{-8} erg s^{-1} cm^{-2})	2.09	1.53
	$F_{\rm diskbb}/F_{\rm tot}$	0.18	0.09
	$F_{\rm comptb}/F_{\rm tot}$	0.79	0.85
	$F_{\rm gauss}/F_{\rm tot}$	0.03	0.06

Notes. Errors are reported at a 68% CL.
[a] Frozen.

NuSTAR. Therefore, in the following spectropolarimetric analysis of the IXPE data, we only considered the `comptt` component.

4. Polarization Analysis

We studied the polarization of Cir X-1 in the three different phase and HR intervals. We first performed a study independent of any spectral model using the `pcube` algorithm of the IXPEOBSSSIM software (Baldini et al. 2022). Then we also studied the polarization applying the spectropolarimetric analysis in XSPEC (Arnaud 1996) by fitting the I, Q, and U spectra. In agreement with the spectral models reported in literature (see, e.g., D'Aì et al. 2012), we describe the I spectrum with the model: `tbabs*comptt`, setting the abundances to the values of Wilms et al. 2000, for the `comptt` model the geometry assumed is a disk (Titarchuk 1994), the hydrogen column density is fixed at the values found in the fit from the previous section for P2 and P3, and for the intermediate value for the HR bins. We did not fit the P1 data, since they are too short, have too few counts for polarimetric studies, and have no contemporaneous NuSTAR data (however, we still studied these data using `pcube`). To take into account IXPE calibration uncertainties (Di Marco et al. 2022b; Rankin et al. 2023), we left the gain slope and offset free, obtaining values, respectively, of the order of 95% for the slope and in the 0.005–0.2 keV range for the offset.

The results for the spectral modeling in the two phase intervals and three HR intervals are reported in Table 3. For the spectropolarimetric analysis, we use the best-fit spectral fits from Table 3 and then fit Q and U using the model `polconst` in XSPEC (see Table 4 for the obtained results). We also attempted fitting with the `pollin` model, but this gave no improvement over `polconst`. We considered fitting with a double `polconst` model (`tbabs*(comptt*polconst + diskbb*polconst)`). However, in this case, due to the low flux of diskbb, not all bins under consideration provide an acceptable fit with all parameters constrained, and we are not able to separate the two components.

4.1. Polarization along the Orbital Phase Intervals

We first studied the PD and PA into each single phase interval in the whole IXPE 2–8 keV energy band. Figure 4 (top) shows a polar plot representing the PD and PA confidence regions in the three phase intervals defined in Figure 1. The polarization in the first phase interval (P1)—the low–hard state—is unconstrained, as expected due to the low counts; the polarization in the remaining two phase intervals—P2 and P3—is significantly detected at a confidence level (CL) higher than 99%. We also observe a clear rotation of the PA by $49° \pm 8°$ between P2 and P3; a 90° rotation is not consistent with this result at a 99.5% CL. The numerical values of polarization obtained in this analysis are reported in Table 5. The results obtained in these phase intervals using XSPEC are summarized in Table 4.

We also attempted to measure the polarization properties in different energy bands (bottom panels of Figure 4). No evidence for an energy dependence at a 90% CL is observed in any energy band; however, there are low-significance hints of a PD energy dependence in P2 and P3. There is also a low-significance indication of a PA rotation with energy in P1; the PA at lower energies is consistent with the PA measured in P3, while at higher energies, it is similar to that of P2.

4.2. Polarization as a Function of HR

Since HR varies during the orbit—even inside the phase intervals we considered above—we studied the polarization in different HR states. This analysis is also useful to have an idea, given the difficulties in the determination of the spectral components, of the polarization of the different emission regions/components. We used the HR values in the time bins of Figure 1 (bottom) to define three different HR intervals: HR1 in the range 0.5–0.6, HR2 in the range 0.6–0.7, and HR3 in the range 0.7–0.8. Given the large uncertainty on each HR value—at a level of ∼0.05—we used the average HR in larger time bins of 2000 s each to populate the three HR intervals in the polarimetric analysis. This average curve is reported in Figure 5 (top).

The polarization computed from events in these HR bins is shown in Figure 5; the numerical values are reported in Table 5, while those obtained with XSPEC are in Table 4. The two estimates are compatible. In the 2–8 keV energy band, the PD is compatible in the three HR intervals, while the PA shows a gradual rotation as the HR changes, with a total rotation of the PA by $67° \pm 11°$ between the lowest and highest HR bins; a 90° rotation is not consistent with this result at a 68.2% CL.

Table 3
Best-fit Parameters Obtained by Fitting IXPE Data with the XSPEC Model `const*tbabs*comptt`

	χ^2/dof	$N_{\rm H}$ (10^{22} cm^{-2}) (fixed)	T_0 (keV)	$kT_{\rm e}$ (keV)	$\tau_{\rm p}$	Norm
P2	417/435	2.77	$0.50^{+0.02}_{-0.04}$	$1.57^{+0.03}_{-0.04}$	11.5 ± 0.4	$1.71^{+0.05}_{-0.04}$
P3	446/435	2.65	$0.59^{+0.04}_{-0.03}$	$2.15^{+0.11}_{-0.09}$	9.4 ± 0.4	$0.77^{+0.03}_{-0.04}$
HR1	404/429	2.7	$0.62^{+0.02}_{-0.08}$	$1.72^{+0.07}_{-0.16}$	$9.1^{+1.4}_{-0.4}$	$1.5^{+0.2}_{-0.1}$
HR2	397/435	2.7	$0.50^{+0.01}_{-0.02}$	$1.68^{+0.02}_{-0.03}$	$11.4^{+0.3}_{-0.1}$	$1.21^{+0.02}_{-0.01}$
HR3	398/433	2.7	$0.61^{+0.03}_{-0.05}$	$2.1^{+0.2}_{-0.1}$	$10.1^{+0.9}_{-0.5}$	$0.88^{+0.02}_{-0.04}$

Note. Uncertainties are at a 68% CL.

Table 4
Polarization Properties Obtained by Fitting the XSPEC Model `const*tbabs*polconst*comptt` to the IXPE I, Q, and U Data

	χ^2/dof	PD (%)	PA (deg)
P2	594/589	1.3 ± 0.2	40 ± 5
P3	603/589	1.1 ± 0.3	-10 ± 7
HR1	609/583	1.1 ± 0.3	43 ± 9
HR2	551/589	1.1 ± 0.2	27 ± 6
HR3	549/587	1.6 ± 0.4	-24 ± 7

Note. Uncertainties are at a 68% CL.

The polarization in different energy bands is reported in Figure 5 (bottom). No evidence for an energy trend at a 90% CL is observed in any energy band, but there are only hints of an increase of PD with energy.

5. Discussion and Conclusions

We studied the X-ray polarization of the NS-XRB Cir X-1 for the first time. With the available statistics, there is no significant variation with energy (see bottom panels of Figures 4 and 5). In other XRBs observed by IXPE, an increase of the PD with energy was observed, but in this case, we only have hints of such an increase; we also find low-significance hints of a rotation of the PA with energy in the hard state at the beginning of the IXPE observation (P1 of Figure 4), which is the state where the Comptonization component is stronger. Comparing with Gnarini et al. (2022) and Poutanen et al. (2023), we find that the energy trend in polarization for the Cir X-1 observation is compatible with a shell or sandwich/wedge coronal geometry (with an inclination of $<80°$) but not a slab geometry, for which a pronounced increase with energy would be expected. However, none of these two scenarios can fully explain our observation, where a change of the polarization is observed as a function of time and HR. This can be explained in terms of a scenario such as the one in Figure 6 (described in more detail below), where an SL and a BL are present, allowing for a deeper analysis capable of estimating the system inclination and the inclination of the NS axis with respect to the disk, but no such model is currently available in the literature.

Along Cir X-1's orbit, we observe a rotation of the PA by $49° \pm 8°$ between different phase intervals (Figure 4), while the PD stays constant within the same observing phase intervals. With the accretion flow expected to be related to the orbital variations of Cir X-1, we perform an analogous study in HR intervals; we also observe in this case a constant PD with a rotation of the PA by $67° \pm 11°$ (Figure 5). The rotation between phase intervals is compatible with the rotation between HRs within a 68% CL.

From a spectral point of view, `comptt` dominates in the IXPE energy band. However, at least two components are present, as reported in Section 3. Thus, the variations along the orbit can be due to a superimposition of two different components contributing in a different way along the phase intervals. Looking at the top panel of Figure 5, we see that all phase intervals are dominated by HR2 (∼60%), with a contribution from HR1 (∼35%) in P2 and from HR3 (∼35%) in P3. This confirms a scenario where the accretion flow—and the HR—varies along the orbit, with the harder state gradually becoming dominant as we get further away from the end of the dip (close to the beginning of the first IXPE observation). This is compatible with a model in which the accretion disk changes during the orbit due to its eccentricity (Johnston et al. 1999). In this model, the modulation in the X-ray luminosity is due to orbital variations in the mass accretion of the compact star; during the periastron passage, the companion star overfills its Roche lobe, and the accretion disk is perturbed through both tidal interaction and a sudden surge of material inflow, triggering an X-ray outburst.

We can interpret variations of the PA as due to two spectral components with significantly different PAs: a lower-energy one dominating at low HR and a harder one dominating at higher HR. In the intermediate HRs, the two components are mixed. Such a two-component model, composed of, e.g., a multicolor blackbody from the accretion disk and a Comptonized component, is the obvious candidate to explain two components in the polarization and so has been proposed for the other IXPE observations of weakly magnetized accreting NSs (Ursini et al. 2023a; Di Marco et al. 2023b; Capitanio et al. 2023; Cocchi et al. 2023; Farinelli et al. 2023). From simple geometrical considerations, and in the absence of relativistic effects, each component can be expected to be polarized either parallel or orthogonal to its symmetry axis. The PA of the optically thick accretion disk is expected to be perpendicular to the position angle of the rotation axis. Relativistic effects may cause a small decrease (for counterclockwise rotation) of the PA by 5°–10° (Loktev et al. 2022). The Comptonization component can be associated either with the BL (which is coplanar with the accretion disk) or with the SL at the NS surface. The PA of the BL is likely nearly aligned with the PA of the accretion disk. In the absence of relativistic effects, the PA of the optically thick SL emission is parallel to the rotation axis. Due to aberration and Doppler boosting, the emission is expected to be dominated by the part of the SL moving toward the observer, breaking the symmetry and causing a decrease (also for counterclockwise rotation) of the PA by up to ∼20°–30° depending on the parameters (A. Bobrikova et al. 2023, in

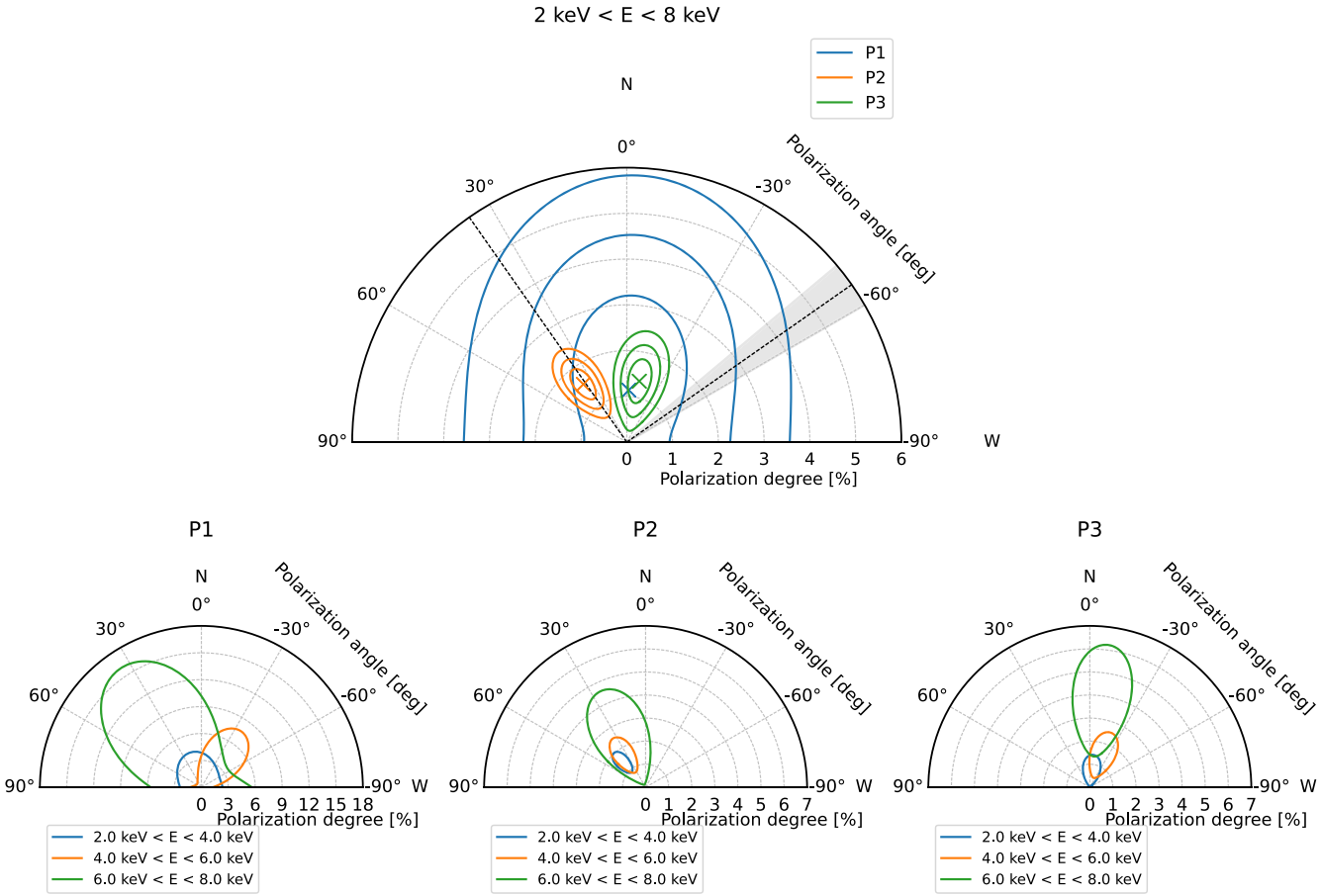

Figure 4. Polar plot of polarization, computed using the `pcube` algorithm from the IXPEOBSSSIM software (Baldini et al. 2022), for the three phase intervals defined in Figure 1. (Top) Polarization in the entire IXPE energy band is reported. The shaded region indicates the direction of the jet (see discussion), and the black lines indicate this direction and its orthogonal direction. Contours are reported at the 68%, 95%, and 99% CLs. (Bottom) Polarization in different energy bands for the three phase intervals, with contours showing the 90% CL.

Table 5
Polarization for Different Phase Intervals and HR Using `pcube`

	PD (%)	PA (deg)	Q/I (%)	U/I (%)	MDP (%)
P1	1.1 ± 1.4	-2 ± 34	1.1 ± 1.4	-0.1 ± 1.4	4.1
P2	1.6 ± 0.3	37 ± 5	0.4 ± 0.3	1.5 ± 0.3	0.79
P3	1.4 ± 0.3	-12 ± 7	1.2 ± 0.3	-0.5 ± 0.3	0.98
HR1	1.6 ± 0.4	40 ± 7	0.2 ± 0.4	1.5 ± 0.4	1.2
HR2	1.3 ± 0.3	24 ± 6	0.9 ± 0.3	1.0 ± 0.3	0.79
HR3	1.9 ± 0.5	-26 ± 7	1.2 ± 0.5	-1.5 ± 0.5	1.5

Note. Uncertainties are at a 68% CL. The minimum detectable polarization (MDP) is the maximum polarization produced by statistical fluctuations at a 99% CL.

preparation). If the SL is optically thin, the PA may rotate by an additional 90° (Sunyaev & Titarchuk 1985; Viironen & Poutanen 2004). However, it is clear from this consideration that the difference in the PA of 50°–60°, as found for Cir X-1, is impossible to produce.

The coexistence of two components with such a large difference in the PA may be explained if their symmetry axes are not aligned. This can be related, for example, to a misalignment of the NS angular momentum with respect to the orbital axis, thus causing a shift of the symmetry axis of the Comptonization region (associated with the SL) with respect to the disk (Abolmasov et al. 2020). We note here that Cir X-1 is not the only source for which such a misalignment might be present, but there are other hints; in Cyg X-2, the PAs of the two components are 66° apart (see Figure 7 in Farinelli et al. 2023), while in XTE J1701−462 and GX 5−1, the difference is ∼40°(Cocchi et al. 2023; Fabiani et al. 2023). Also, X-ray polarimetry provided evidence for a misalignment in the X-ray pulsar Her X-1 (Doroshenko et al. 2022). Such a misalignment is in fact more likely for Cir X-1 than for other NS systems, as the system is younger than 4600 yr (Heinz et al. 2013); if the newly formed NS spins out of plane with respect to the binary system, there is not enough time to come to the alignment of the spinning axes.

At the same time, the accretion disk itself has a lower temperature compared to the Comptonization components (Iaria et al. 2008) and does not contribute significantly to the IXPE band. Thus, the only other option for the second component is the BL. At low accretion rates (Figure 6, left), the disk is terminated at the innermost stable orbit of ∼3 Schwarzschild radii (i.e., about 13.5 km for a 1.5 $M_\odot$ NS), which is likely larger than the NS radius of ∼12 km (e.g., Nättilä et al. 2017; Annala et al. 2022). In this situation, the BL does not exist at all, and matter freefalls on the NS surface, forming an SL. Thus, the PA would correspond to the orientation of the NS rotation axis on the sky. At high accretion rates (Figure 6, right), the thickness of the SL grows, connecting it to the accretion disk through the BL. In this case, the PA would be related to the symmetry axis of the disk.

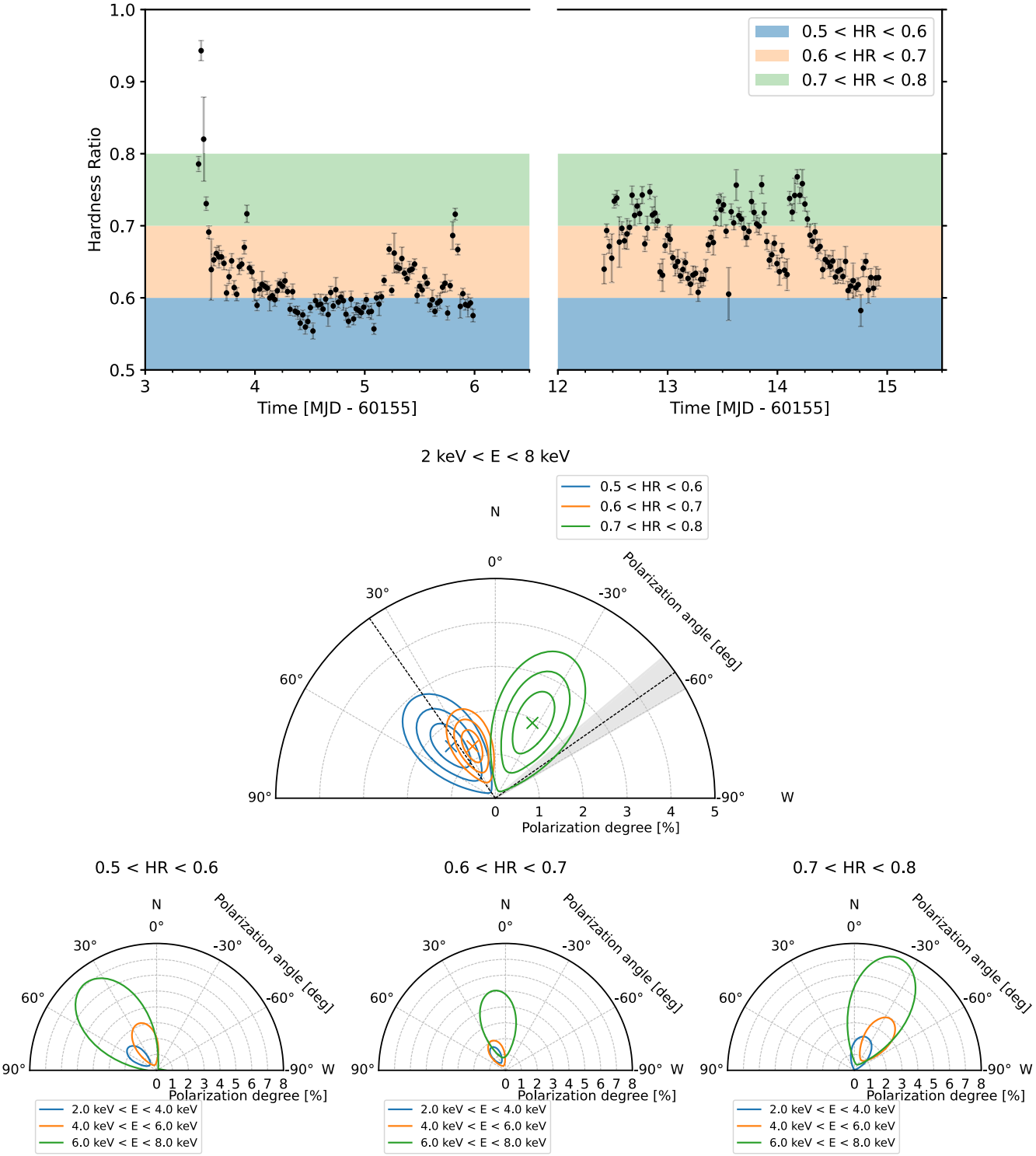

Figure 5. Study of polarization binned in HR. (Top) HR trend with time (2000 s time binning); the colored bands identify the chosen binning for HR. (Middle) Polar plot of polarization, computed using the model-independent `pcube` algorithm from the IXPEOBSSSIM software (Baldini et al. 2022), for events in different intervals of HR reported in the top panel in the energy band 2–8 keV, where the shaded region indicates the direction of the jet (see discussion), and the black lines indicate this direction and its orthogonal direction. Contours are reported at 68%, 95%, and 99% CLs. (Bottom) Polarization in different energy bands. Contours are reported at a 90% CL.

Tominaga et al. (2023) modeled Cir X-1 as an accretion disk covered by a partially covering medium and interpreted the different phases of the orbit as changes in these two components. Their observations cover the dip for much longer than the IXPE polarimetric ones, where there is no significant polarimetric information for this phase; if we had observed the dip for longer with IXPE, we might have expected a high PD due to obscuration, as observed in black hole systems (Ursini et al. 2023b; Veledina et al. 2023). It is interesting to note how their model is very good at predicting observational features

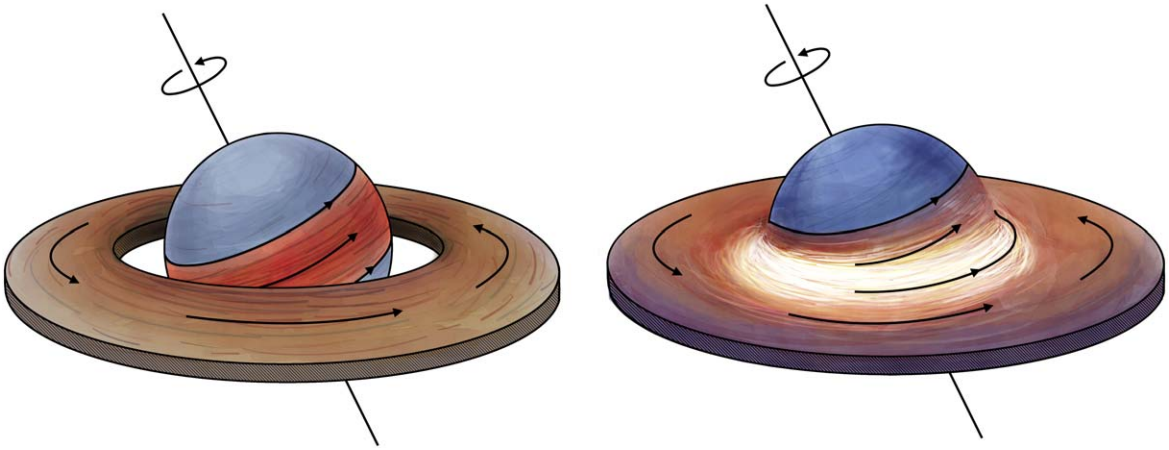

Figure 6. Illustration of a possible accretion geometry in Cir X-1. (Left) Low accretion rate case, when there is a gap between the disk and the NS surface, and the full SL is developed. (Right) High accretion rate case, where the disk touches the NS surface, and the BL is emitting (with a PA almost perpendicular to the symmetry axis of the disk).

such as lines, while to interpret the polarization, we need a geometric model dealing with different features, such as the model we outlined in this paper.

In order to understand the geometry of the inner accretion flow in Cir X-1, it is now worth relating the observed PAs to the orientation of the jet. Cir X-1 is among the few NS-XRBs showing jets in both the radio and the X-ray. The position angle of the (approaching) jet measured in the radio lies in the range 110°–140° (Fender et al. 1998; Tudose et al. 2008; Sell et al. 2010; Calvelo et al. 2012; Miller-Jones et al. 2012). Also in the X-ray, the signature of the (receding) jet is found in the northwest direction at position angles of about −70° and −35° (Heinz et al. 2007; Soleri et al. 2009), while the approaching jet is seen in the PA interval of 90°–150° (Soleri et al. 2009). Thus, the average jet direction seems to be nearly orthogonal to the direction of the X-ray polarization in P2 (and at H1 and H2; see Table 5), which we associate with the BL emission. On the other hand, the X-ray polarization at the highest HR (HR3) is $\sim 1.3\sigma$ apart from the jet direction (−35° or 140°–150°). Finally, the X-ray PA of −12° during P3 is clearly neither parallel nor perpendicular to the jet. Associating the observed PA with the SL implies a misalignment of the NS's angular momentum from the orbital axis by about 30° (Figure 6). Because the PA in this case is larger than the jet position angle, the rotation of the SL (and the disk) has to be clockwise, corresponding to an inclination exceeding 90°.

Although a large spread in the position angles measured for the jet can be explained by precession (Sell et al. 2010; Calvelo et al. 2012), such an interpretation does not work for the variations of the X-ray PAs because of the much shorter timescales involved and the detection of different PAs at different HRs. This gives further support to the interpretation that variations of the PA are caused by different spectral components (accretion disk, BL, and SL) dominating at different times. With the data at hand, it is impossible to extract those components from the spectra; variations of the PA, however, strongly support the idea that the NS angular momentum is misaligned from the orbital one, which is a necessary requirement for the precession to operate. The X-ray polarimetric data thus provide a unique view of the geometry of the accreting NS Cir X-1.

Acknowledgments

The Imaging X-ray Polarimetry Explorer (IXPE) is a joint US and Italian mission. The US contribution is supported by the National Aeronautics and Space Administration (NASA) and led and managed by its Marshall Space Flight Center (MSFC), with industry partner Ball Aerospace (contract NNM15AA18C). The Italian contribution is supported by the Italian Space Agency (Agenzia Spaziale Italiana, ASI) through contract ASI-OHBI-2022-13-I.0, agreements ASI-INAF-2022-19-HH.0 and ASI-INFN-2017.13-H0, and its Space Science Data Center (SSDC) with agreements ASI-INAF-2022-14-HH.0 and ASI-INFN 2021-43-HH.0, as well as by the Istituto Nazionale di Astrofisica (INAF) and the Istituto Nazionale di Fisica Nucleare (INFN) in Italy. This research used data products provided by the IXPE Team (MSFC, SSDC, INAF, and INFN) and distributed with additional software tools by the High-Energy Astrophysics Science Archive Research Center (HEASARC) at NASA Goddard Space Flight Center (GSFC). This research has made use of the MAXI data provided by RIKEN, JAXA, and the MAXI team.

We acknowledge support from Academy of Finland grants 333112, 355672, and 349144 (J.P., A.V., S.S.T.) and the German Academic Exchange Service (DAAD) travel grant 57525212 (V.D.). V.Kr. acknowledges support from the Finnish Cultural Foundation. F.A. and A.P. acknowledge financial support from the INAF Research Grant "Uncovering the optical beat of the fastest magnetized neutron stars (FANS)" and the Italian Ministry of University and Research (MUR), PRIN 2020 (prot. 2020BRP57Z), "Gravitational and Electromagnetic-wave Sources in the Universe with current and next-generation detectors (GEMS)." I.L. was supported by the NASA postdoctoral program at the Marshall Space Flight Center, administered by Oak Ridge Associated Universities under contract with NASA. F.X. is supported by the National Key R&D Program of China (grant No. 2023YFE0117200) and by the National Natural Science Foundation of China (grant No. 12373041).

Facilities: IXPE, NICER, NuSTAR, MAXI.

Software: IXPEOBSSIM (Baldini et al. 2022), XSPEC (Arnaud 1996), HEASOFT (Nasa Heasarc 2014).

ORCID iDs

John Rankin https://orcid.org/0000-0002-9774-0560
Fabio La Monaca https://orcid.org/0000-0001-8916-4156
Alessandro Di Marco https://orcid.org/0000-0003-0331-3259
Juri Poutanen https://orcid.org/0000-0002-0983-0049
Anna Bobrikova https://orcid.org/0009-0009-3183-9742
Vadim Kravtsov https://orcid.org/0000-0002-7502-3173
Fabio Muleri https://orcid.org/0000-0003-3331-3794
Maura Pilia https://orcid.org/0000-0001-7397-8091
Alexandra Veledina https://orcid.org/0000-0002-5767-7253
Rob Fender https://orcid.org/0000-0002-5654-2744
Philip Kaaret https://orcid.org/0000-0002-3638-0637
Dawoon E. Kim https://orcid.org/0000-0001-5717-3736
Andrea Marinucci https://orcid.org/0000-0002-2055-4946
Herman L. Marshall https://orcid.org/0000-0002-6492-1293
Alessandro Papitto https://orcid.org/0000-0001-6289-7413
Allyn F. Tennant https://orcid.org/0000-0002-9443-6774
Sergey S. Tsygankov https://orcid.org/0000-0002-9679-0793
Martin C. Weisskopf https://orcid.org/0000-0002-5270-4240
Kinwah Wu https://orcid.org/0000-0002-7568-8765
Silvia Zane https://orcid.org/0000-0001-5326-880X
Filippo Ambrosino https://orcid.org/0000-0001-7915-996X
Ruben Farinelli https://orcid.org/0000-0003-2212-367X
Andrea Gnarini https://orcid.org/0000-0002-0642-1135
Iván Agudo https://orcid.org/0000-0002-3777-6182
Lucio A. Antonelli https://orcid.org/0000-0002-5037-9034
Matteo Bachetti https://orcid.org/0000-0002-4576-9337
Luca Baldini https://orcid.org/0000-0002-9785-7726
Wayne H. Baumgartner https://orcid.org/0000-0002-5106-0463
Ronaldo Bellazzini https://orcid.org/0000-0002-2469-7063
Stefano Bianchi https://orcid.org/0000-0002-4622-4240
Stephen D. Bongiorno https://orcid.org/0000-0002-0901-2097
Raffaella Bonino https://orcid.org/0000-0002-4264-1215
Alessandro Brez https://orcid.org/0000-0002-9460-1821
Niccolò Bucciantini https://orcid.org/0000-0002-8848-1392
Fiamma Capitanio https://orcid.org/0000-0002-6384-3027
Simone Castellano https://orcid.org/0000-0003-1111-4292
Elisabetta Cavazzuti https://orcid.org/0000-0001-7150-9638
Chien-Ting Chen https://orcid.org/0000-0002-4945-5079
Stefano Ciprini https://orcid.org/0000-0002-0712-2479
Enrico Costa https://orcid.org/0000-0003-4925-8523
Alessandra De Rosa https://orcid.org/0000-0001-5668-6863
Ettore Del Monte https://orcid.org/0000-0002-3013-6334
Laura Di Gesu https://orcid.org/0000-0002-5614-5028
Niccolò Di Lalla https://orcid.org/0000-0002-7574-1298
Immacolata Donnarumma https://orcid.org/0000-0002-4700-4549
Victor Doroshenko https://orcid.org/0000-0001-8162-1105
Michal Dovčiak https://orcid.org/0000-0003-0079-1239
Steven R. Ehlert https://orcid.org/0000-0003-4420-2838
Teruaki Enoto https://orcid.org/0000-0003-1244-3100
Yuri Evangelista https://orcid.org/0000-0001-6096-6710
Sergio Fabiani https://orcid.org/0000-0003-1533-0283
Riccardo Ferrazzoli https://orcid.org/0000-0003-1074-8605
Javier A. Garcia https://orcid.org/0000-0003-3828-2448
Shuichi Gunji https://orcid.org/0000-0002-5881-2445
Jeremy Heyl https://orcid.org/0000-0001-9739-367X
Wataru Iwakiri https://orcid.org/0000-0002-0207-9010
Svetlana G. Jorstad https://orcid.org/0000-0001-6158-1708
Vladimir Karas https://orcid.org/0000-0002-5760-0459
Fabian Kislat https://orcid.org/0000-0001-7477-0380
Jeffery J. Kolodziejczak https://orcid.org/0000-0002-0110-6136
Henric Krawczynski https://orcid.org/0000-0002-1084-6507
Luca Latronico https://orcid.org/0000-0002-0984-1856
Ioannis Liodakis https://orcid.org/0000-0001-9200-4006
Simone Maldera https://orcid.org/0000-0002-0698-4421
Alberto Manfreda https://orcid.org/0000-0002-0998-4953
Frédéric Marin https://orcid.org/0000-0003-4952-0835
Alan P. Marscher https://orcid.org/0000-0001-7396-3332
Francesco Massaro https://orcid.org/0000-0002-1704-9850
Giorgio Matt https://orcid.org/0000-0002-2152-0916
Tsunefumi Mizuno https://orcid.org/0000-0001-7263-0296
Michela Negro https://orcid.org/0000-0002-6548-5622
Chi-Yung Ng https://orcid.org/0000-0002-5847-2612
Stephen L. O'Dell https://orcid.org/0000-0002-1868-8056
Nicola Omodei https://orcid.org/0000-0002-5448-7577
Chiara Oppedisano https://orcid.org/0000-0001-6194-4601
George G. Pavlov https://orcid.org/0000-0002-7481-5259
Abel L. Peirson https://orcid.org/0000-0001-6292-1911
Matteo Perri https://orcid.org/0000-0003-3613-4409
Melissa Pesce-Rollins https://orcid.org/0000-0003-1790-8018
Pierre-Olivier Petrucci https://orcid.org/0000-0001-6061-3480
Andrea Possenti https://orcid.org/0000-0001-5902-3731
Simonetta Puccetti https://orcid.org/0000-0002-2734-7835
Brian D. Ramsey https://orcid.org/0000-0003-1548-1524
Ajay Ratheesh https://orcid.org/0000-0003-0411-4243
Oliver J. Roberts https://orcid.org/0000-0002-7150-9061
Roger W. Romani https://orcid.org/0000-0001-6711-3286
Carmelo Sgrò https://orcid.org/0000-0001-5676-6214
Patrick Slane https://orcid.org/0000-0002-6986-6756
Paolo Soffitta https://orcid.org/0000-0002-7781-4104
Gloria Spandre https://orcid.org/0000-0003-0802-3453
Douglas A. Swartz https://orcid.org/0000-0002-2954-4461
Toru Tamagawa https://orcid.org/0000-0002-8801-6263
Fabrizio Tavecchio https://orcid.org/0000-0003-0256-0995
Roberto Taverna https://orcid.org/0000-0002-1768-618X
Nicholas E. Thomas https://orcid.org/0000-0003-0411-4606
Francesco Tombesi https://orcid.org/0000-0002-6562-8654
Alessio Trois https://orcid.org/0000-0002-3180-6002
Roberto Turolla https://orcid.org/0000-0003-3977-8760
Jacco Vink https://orcid.org/0000-0002-4708-4219
Fei Xie https://orcid.org/0000-0002-0105-5826

References

Abolmasov, P., Nättilä, J., & Poutanen, J. 2020, A&A, 638, A142
Annala, E., Gorda, T., Katerini, E., et al. 2022, PhRvX, 12, 011058
Arnaud, K. A. 1996, in ASP Conf. Ser. 101, Astronomical Data Analysis Software and Systems V, ed. G. H. Jacoby & J. Barnes (San Francisco: ASP), 17
Baldini, L., Barbanera, M., Bellazzini, R., et al. 2021, APh, 133, 102628
Baldini, L., Bucciantini, N., Lalla, N. D., et al. 2022, SoftX, 19, 101194
Bellazzini, R., Spandre, G., Minuti, M., et al. 2006, NIMPA, 566, 552

Bellazzini, R., Spandre, G., Minuti, M., et al. 2007, NIMPA, 579, 853
Calvelo, D. E., Fender, R. P., Tzioumis, A. K., & Broderick, J. W. 2012, MNRAS, 419, L54
Capitanio, F., Fabiani, S., Gnarini, A., et al. 2023, ApJ, 943, 129
Cocchi, M., Gnarini, A., Fabiani, S., et al. 2023, A&A, 674, L10
Connors, P. A., Piran, T., & Stark, R. F. 1980, ApJ, 235, 224
Connors, P. A., & Stark, R. F. 1977, Natur, 269, 128
Coriat, M., Fender, R. P., Tasse, C., et al. 2019, MNRAS, 484, 1672
Costa, E., Soffitta, P., Bellazzini, R., et al. 2001, Natur, 411, 662
D'Aì, A., Bozzo, E., Papitto, A., et al. 2012, A&A, 543, A20
Di Marco, A., Costa, E., Muleri, F., et al. 2022a, AJ, 163, 170
Di Marco, A., Muleri, F., Fabiani, S., et al. 2022b, Proc. SPIE, 12181, 121811C
Di Marco, A., Soffitta, P., Costa, E., et al. 2023a, AJ, 165, 143
Di Marco, A., La Monaca, F., Poutanen, J., et al. 2023b, ApJL, 953, L22
Doroshenko, V., Poutanen, J., Tsygankov, S. S., et al. 2022, NatAs, 6, 1433
Dovčiak, M., Karas, V., & Matt, G. 2004, MNRAS, 355, 1005
Fabiani, S., Capitanio, F., Iaria, R., et al. 2023, arXiv:2310.06788
Farinelli, R., Fabiani, S., Poutanen, J., et al. 2023, MNRAS, 519, 3681
Fender, R., Spencer, R., Tzioumis, T., et al. 1998, ApJL, 506, L121
Fender, R., Wu, K., Johnston, H., et al. 2004, Natur, 427, 222
Gendreau, K. C., Arzoumanian, Z., Adkins, P. W., et al. 2016, Proc. SPIE, 9905, 99051H
Gnarini, A., Ursini, F., Matt, G., et al. 2022, MNRAS, 514, 2561
Harrison, F. A., Craig, W. W., Christensen, F. E., et al. 2013, ApJ, 770, 103
Hasinger, G., & van der Klis, M. 1989, A&A, 225, 79
Heinz, S., Schulz, N. S., Brandt, W. N., & Galloway, D. K. 2007, ApJL, 663, L93
Heinz, S., Sell, P., Fender, R. P., et al. 2013, ApJ, 779, 171
Iaria, R., Di Salvo, T., Robba, N. R., & Burderi, L. 2002, ApJ, 567, 503
Iaria, R., Spanò, M., Di Salvo, T., et al. 2005, ApJ, 619, 503
Iaria, R., Spanò, M., Di Salvo, T., et al. 2008, ApJ, 619, 503
Inogamov, N. A., & Sunyaev, R. A. 1999, AstL, 25, 269
Johnston, H. M., Fender, R., & Wu, K. 1999, MNRAS, 308, 415
Kaluzienski, L. J., Holt, S. S., Boldt, E. A., & Serlemitsos, P. J. 1976, ApJL, 208, L71
Kislat, F., Clark, B., Beilicke, M., & Krawczynski, H. 2015, APh, 68, 45
Linares, M., Watts, A., Altamirano, D., et al. 2010, ApJL, 719, L84
Loktev, V., Salmi, T., Nättilä, J., & Poutanen, J. 2020, A&A, 643, A84
Loktev, V., Veledina, A., & Poutanen, J. 2022, A&A, 660, A25
Madsen, K. K., Forster, K., Grefenstette, B., Harrison, F. A., & Miyasaka, H. 2022, JATIS, 8, 034003
Makishima, K., Maejima, Y., Mitsuda, K., et al. 1986, ApJ, 308, 635
Matsuoka, M., Kawasaki, K., Ueno, S., et al. 2009, PASJ, 61, 999
Miller-Jones, J. C. A., Moin, A., Tingay, S. J., et al. 2012, MNRAS, 419, L49
Mitsuda, K., Inoue, H., Koyama, K., et al. 1984, PASJ, 36, 741
Nasa Heasarc, 2014 HEAsoft: Unified Release of FTOOLS and XANADU, Astrophysics Source Code Library, ascl:1408.004
Nättilä, J., Miller, M. C., Steiner, A. W., et al. 2017, A&A, 608, A31
Popham, R., & Sunyaev, R. 2001, ApJ, 547, 355
Poutanen, J., Veledina, A., & Beloborodov, A. M. 2023, ApJL, 949, L10
Rankin, J., Muleri, F., Ferrazzoli, R., et al. 2023, Proc. SPIE, 12678, 126780D
Schulz, N. S., Kallman, T. E., Heinz, S., et al. 2019, IAUS, 346, 125
Schulz, N. S., Kallman, T. E., Heinz, S., et al. 2020, ApJ, 891, 150
Sell, P. H., Heinz, S., Calvelo, D. E., et al. 2010, ApJL, 719, L194
Shakura, N. I., & Sunyaev, R. A. 1988, AdSpR, 8, 135
Soffitta, P., Baldini, L., Bellazzini, R., et al. 2021, AJ, 162, 208
Soleri, P., Heinz, S., Fender, R., et al. 2009, MNRAS, 397, L1
Suleimanov, V., & Poutanen, J. 2006, MNRAS, 369, 2036
Sunyaev, R. A., & Titarchuk, L. G. 1985, A&A, 143, 374
Tennant, A. F., Fabian, A. C., & Shafer, R. A. 1986, MNRAS, 221, 27P
Titarchuk, L. 1994, Generalized comptonization models and application to the recent high energy observations, in AIP Conf. Proc. 304 (San Francisco, CA: ASP), 380
Titarchuk, L. 1994, ApJ, 434, 570
Tominaga, M., Tsujimoto, M., Ebisawa, K., Enoto, T., & Hayasaki, K. 2023, ApJ, 958, 52
Tudose, V., Fender, R. P., Tzioumis, A. K., Spencer, R. E., & van der Klis, M. 2008, MNRAS, 390, 447
Ursini, F., Farinelli, R., Gnarini, A., et al. 2023a, A&A, 676, A20
Ursini, F., Marinucci, A., Matt, G., et al. 2023b, MNRAS, 519, 50
van der Klis, M. 1989, ARA&A, 27, 517
Veledina, A., Muleri, F., Poutanen, J., et al. 2023, arXiv:2303.01174
Viironen, K., & Poutanen, J. 2004, A&A, 426, 985
Weisskopf, M. C., Soffitta, P., Baldini, L., et al. 2022, JATIS, 8, 026002
Wilms, J., Allen, A., & McCray, R. 2000, ApJ, 542, 914